SCIENCE CHINA
Chemistry

•ARTICLES•

December 2021 Vol.64 No.12: 2118–2124
https://doi.org/10.1007/s11426-021-1060-3

Core engineering of paired core-shell silver nanoclusters

Shan-Shan Zhang[1], Rui-Chen Liu[1], Xiao-Chen Zhang[1], Lei Feng[1], Qing-Wang Xue[3], Zhi-Yong Gao[2], Chen-Ho Tung & Di Sun[1*]

[1]*Key Lab of Colloid and Interface Chemistry, Ministry of Education, School of Chemistry and Chemical Engineering, State Key Laboratory of Crystal Materials, Shandong University, Jinan 250100, China;*
[2]*School of Chemistry and Chemical Engineering, Collaborative Innovation Center of Henan Province for Green Manufacturing of Fine Chemicals, Key Laboratory of Green Chemical Media and Reactions, Ministry of Education, Henan Normal University, Xinxiang 453007, China;*
[3]*Shandong Provincial Key Laboratory of Chemical Energy Storage and Novel Cell Technology, School of Chemistry and Chemical Engineering, Liaocheng University, Liaocheng 252000, China*

Received May 25, 2021; accepted June 25, 2021; published online September 17, 2021

Unlike the facile modulation of surface structure through protecting ligands, the core shielded by outer shell of silver nanoclusters is still hard to be controlled. Ligand effects may seep into the incipient growth of silver core. However, the comparable cases to validate such hypothesis are currently lacking. Herein, we shed light on two core-shell silver nanoclusters, $Ag_7S_6@Ag_{48}$ (**SD/Ag55b**, SD = SunDi) and $Ag_6S_6@Ag_{48}$ (**SD/Ag54b**), differing in only one silver atom in the core which varies from a pentagon-bipyramidal Ag_7 to an octahedral Ag_6 while keeping the Ag_{48} shielding shell almost the same. Although no direct bonding between alkynes and silver core is observed in them, we propose that the ligand effect still exerts profound influences on the size and geometry of silver core. The solution behaviours and complete ligand-exchange reaction of **SD/Ag55b** in CH_2Cl_2 are investigated using electrospray ionization mass spectrometry. Due to more and stronger argentophilic interactions, **SD/Ag55b** exhibits room-temperature phosphorescence with a 40 nm red-shift compared to that of **SD/Ag54b** in CH_2Cl_2. This work not only presents effective fabrication of silver nanoclusters *via* synergism of dithiophosphate and alkyne ligands, but also provides us a pair of comparable examples to understand substitution group effect of protecting ligand on the core structures and properties.

silver nanocluster, core engineering, argentophilic interactions, red-shifted phosphorescence, dynamic ligand exchange

Citation: Zhang SS, Liu RC, Zhang XC, Feng L, Xue QW, Gao ZY, Tung CH, Sun D. Core engineering of paired core-shell silver nanoclusters. *Sci China Chem*, 2021, 64: 2118–2124, https://doi.org/10.1007/s11426-021-1060-3

1 Introduction

Ligand-protected silver nanoclusters continue to experience scientific interest and curiosity owing to their aesthetic structures, size-dependent physicochemical properties and special role as a bridge between individual metal atoms and larger nanoparticles [1–11]. The synthetic chemistry, crystallization, and assembly mechanism of silver nanoclusters remain three eternal themes full of challenges in this field. In the syntheses of atom-precise silver nanoclusters, several kinds of organics have been developed as preponderant protecting ligand, such as alkynes, carbene, *N*-heterocyclic compounds, thiolates and phosphine ligands, owing to their synthetic tunability and accessibility, ease of handling, and versatile binding sites/modes [12–24]. In contrast, P/S ligands are much less used in metal nanoclusters [25,26]. Although dithiophosphate ligands are formally monovalent anions, they are strong chelating clamps due to two adjacent

*Corresponding author (email: dsun@sdu.edu.cn)

S atoms with each bonded to two silver atoms, which makes them more beneficial to shape silver tetragons than alkynes and thiolates [27]. Due to such a feature of dithiophosphate in constructing silver polygons, polyhedral silver nanoclusters built from these basic units are usually anticipated with charming aesthetic appeal and high symmetry. Up to now, notable progress of dithiophosphate-protected silver/copper clusters has been made by Liu group [28] who isolated $\{Ag_{21}[S_2P(O^iPr)_2]_{12}\}^+$, $\{Ag_{20}[S_2P(OR)_2]_{12}\}$ (R = Pr or ^{i}Pr) [29], $\{Ag_7(H)[S_2P(OEt)_2]_6\}$ [30], $\{Ag_9(S)[S_2P(OEt)_2]_8\}^-$ [31], $[Cu_{28}H_{15}(S_2CNR_2)_{12}]^+$ (NR=N^{n}Pr$_2$ or aza-15-crown-5) [32] and $\{Cu_{32}H_{20}[S_2P(O^iPr)_2]_{12}\}$ [33] *etc*. Moreover, some platinum/palladium-doped silver nanoclusters such as $[Pt_3Ag_{44}(S_2P(O^iPr)_2)_{22}]$ and $\{Pd_6Ag_{14}(S)[S_2P(O^nPr)_2]_{12}\}$ were also documented by the same group [34,35]. The most contributions of dithiophosphate to the development of silver nanoclusters have been involved in above works, although the earlier research can be traced back to 2005 [36,37]. Thus, introducing dithiophosphates with or without other auxiliary ligands into assembly of silver nanoclusters may bring new opportunities to explore novel members in this family.

Among silver nanocluster family, there is an interesting subgroup featuring core-shell hierarchical structures [38,39]. The formation of them has reached a consensus that the growth of metal core is a kinetics controlled process followed by the encapsulation of outer silver shell to finally give a thermodynamically stable product. The former is influenced by all possible assembly factors such as solvents, temperature, and ligands. However, no examples can unveil the details underlying such a transient core growth stage. It should be noted that the active metal core has very short lifetime and thus will be quickly passivated by accessible coordination species. Our and other groups reported several cases of core-shell silver nanoclusters with different core geometries and sizes such as $[Ag_6@Ag_{52}]$, $[Ag_6@Ag_{56}]$, $[Ag_6@Ag_{60}]$, $[Ag_{10}@Ag_{70}]$, $[Ag_{10}@Ag_{74}]$, $[Ag_{10}@Ag_{60}]$, $[Ag_{11}@Ag_{44}]$, $[Ag_{11}@Ag_{43}]$, $[Ag_7@Ag_{37}]$, $[Ag_{14}S_{13}@Ag_{48}]$, $[Ag_{14}S_{12}@Ag_{42}]$, $[Ag_4S_4@Ag_{66}]$, and $[Ag_6S_4@Ag_{36}]$ [40–49]. From these examples, we can see that some small anions such as MoO_4^{2-}, CO_3^{2-}, and S^{2-} usually passivate the inner silver cores and participate in the formation of the final solid structures [40,42,44–46], while organic ligands have never been seen to directly ligate with these cores. However, could it be that the organic ligands really did not have any influences on the formation of silver core in the early stage? This is an important scientific issue needing some comparable examples to answer.

Motivated by above discussions, herein, we adopt a mixed-ligand approach and take advantages of both $Ph_2PS_2^-$ and $RC{\equiv}C^-$ ligands to the assembly of silver nanoclusters. Two nanoclusters, $[Ag_7S_6@Ag_{48}(MoO_4)_2(p\text{-}MePhC{\equiv}C)_{24}(Ph_2PS_2)_{12}]\cdot 3CF_3SO_3\cdot 4CH_3OH\cdot 2H_2O$ (**SD/Ag55b**) and $[Ag_6S_6@Ag_{48}(MoO_4)_2(PhC{\equiv}C)_{24}(Ph_2PS_2)_{12}]\cdot 2CF_3SO_3$ (**SD/Ag54b**), show different cores but similar Ag_{48} shells. It is worth noting that the $Ph_2PS_2^-$ and $RC{\equiv}C^-$ ligands specifically shape silver tetragons and trigons of Ag_{48} shells, respectively. More important, the different core structures (Ag_7S_6 *vs*. Ag_6S_6) are obviously dictated by different substitute group of alkynes ligands (*p*-MePhC≡C$^-$ *vs*. PhC≡C$^-$). This work enables us to accurately understand the individual effect of dithiophosphate and alkyne ligands in the construction of sophisticated core-shell silver nanoclusters, as well as the influences of substitute group ligands on the nucleation and configuration of the cores.

2 Results and discussion

2.1 Synthesis discussions

Experimental details including the synthesis, isolation, X-ray single-crystal diffraction (SCXRD), infrared spectra (IR), nuclear magnetic resonance spectroscopy (NMR), powder X-ray diffraction (PXRD), energy dispersive X-ray spectrometry (EDS) and ultraviolet-visible spectroscopy (UV-Vis) (Figures S1–S27, and Tables S1–S3) are shown in the Supporting Information online.

SD/Ag55b and **SD/Ag54b** were synthesized through a facile one-pot solvothermal reaction of silver-alkyne polymeric precursors, silver salts, $Ph_2PS_2{\cdot}HNEt_3$ [50] and molybdates in methanol (Scheme 1). The details of the optimal syntheses of **SD/Ag55b** and **SD/Ag54b** are given in the Supporting Information online. In this system, we have tried different silver salts, molybdate templates, solvents and reaction conditions to optimize the synthetic parameters. It was found that **SD/Ag55b** and **SD/Ag54b** could be isolated by using $Na_2MoO_4{\cdot}2H_2O$, $(NH_4)_6Mo_7O_{24}{\cdot}4H_2O$ or $H_6CrMo_6O_{24}$ as template sources and CH_3OH or CH_3OH/DMF as solvent systems. Moreover, crystals can only be obtained under the conditions of low-temperature solvothermal reaction at 70 °C. The target product cannot be obtained by stirring or ultrasound at room temperature or 70 °C (Table S1). Their samples were collected as orange rod crystals from the bottom and wall of the vial and the yields of them can reach up to ~50%.

2.2 X-ray crystal structures

The molecular structures of **SD/Ag55b** and **SD/Ag54b** were determined as $[Ag_7S_6@Ag_{48}(MoO_4)_2(p\text{-}MePhC{\equiv}C)_{24}(Ph_2PS_2)_{12}]\cdot 3CF_3SO_3\cdot 4CH_3OH\cdot 2H_2O$ (Figure 1a) and $[Ag_6S_6@Ag_{48}(MoO_4)_2(PhC{\equiv}C)_{24}(Ph_2PS_2)_{12}]\cdot 2CF_3SO_3$ (Figure 1b), respectively, by SCXRD analyses (Table S2). **SD/Ag55b** and **SD/Ag54b** crystallized into monoclinic $P2_1/n$ and triclinic P-1 space group, respectively. Their asymmetric units contain only a half of cluster imposed by inversion center. Interestingly, **SD/Ag55b** and **SD/Ag54b** have a very similar

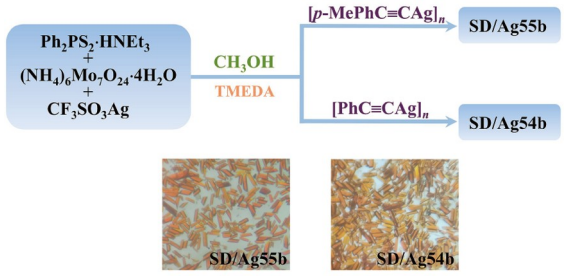

Scheme 1 Synthetic routes for **SD/Ag55b** and **SD/Ag54b** (TMEDA = *N*,*N*,*N*′,*N*′-tetramethylethane-1,2-diamine) (color online).

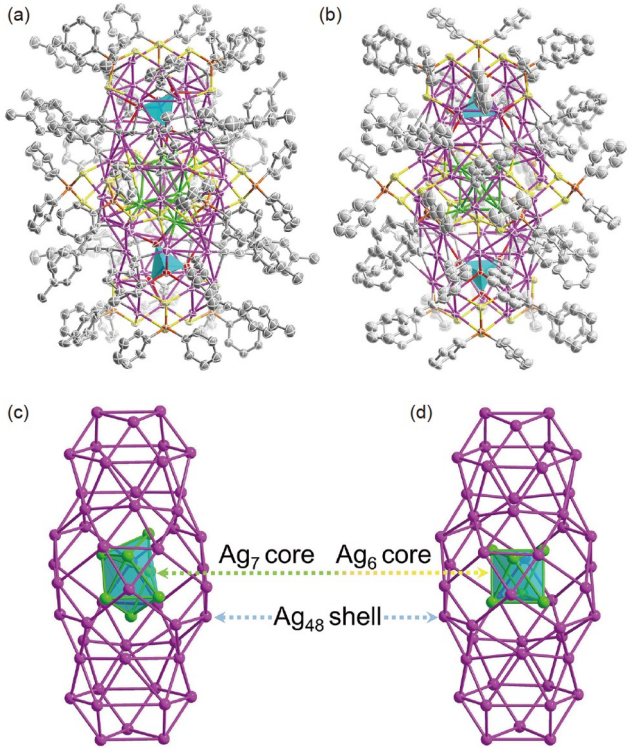

Figure 1 Total cluster structure of **SD/Ag55b** (a) and **SD/Ag54b** (b). Thermal ellipsoids are drawn at the 50% probability level. Hydrogen atoms are removed for clarity. MoO_4^{2-} is shown as cyan tetrahedron. Comparison between the silver framework of **SD/Ag55b** (c) and **SD/Ag54b** (d). Color legend: Ag, purple/green; P, orange; S, yellow; O, red; C, gray (color online).

Ag_{48} shell and the same ligands binding motifs but quite different cores (Figure 1c, d).

The rod-like **SD/Ag55b** contains 55 silver atoms, 24 *p*-MePhC≡C$^-$, 12 $Ph_2PS_2^-$, 6 S^{2-} and 2 MoO_4^{2-}. The 55 Ag atoms can be divided into two categories: 48 on the outer shell (Ag_{48} shell) and the remaining 7 in the core (Ag_7 core). The Ag···Ag distances within Ag_{48} shell and Ag_7 core as well as those between the two layers fall in the ranges of 2.85–3.41, 2.85–3.28 and 2.86–3.39 Å, respectively, indicating important argentophilic interactions [51–53]. The Ag_{48} shell can be seen as two Ag_{15} cages at two ends sandwiching an Ag_{30} cage at the waist through face-shared silver hexagons (cyan rings in Figure 2a). Each Ag_{15} cage consists

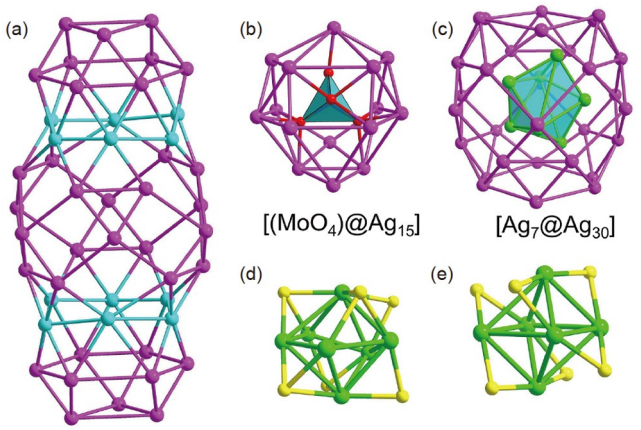

Figure 2 (a) The Ag_{48} shell of **SD/Ag55b**. The structure of $[(MoO_4)@Ag_{15}]$ (b) and $[Ag_7@Ag_{30}]$ (c) in **SD/Ag55b**. MoO_4^{2-} is shown as cyan tetrahedron. (d) The Ag_7S_6 core in **SD/Ag55b**. (e) The Ag_6S_6 core in **SD/Ag54b**. Color legend: Ag, purple/cyan/green; S, yellow; O, red; Mo, blue (color online).

of 16 trigons, 3 tetragons and 1 hexagon as base, whereas Ag_{30} cage is comprised of 24 trigons, 12 tetragons and 2 hexagons. In each Ag_{15} cage, one tetrahedral MoO_4^{2-} is encapsulated and interacts with Ag atoms by μ_2 and μ_3 O atoms with the Ag–O distances in 2.34–2.74 Å (Figure 2b), whereas a distorted pentagon-bipyramidal Ag_7 is shielded by the Ag_{30} cage (Figure 2c). The innermost seven silver atoms and six capping S^{2-} ions form an Ag_7S_6 core (Figure 2d) which connects to the outer Ag_{30} cage through Ag–S bonds (Ag–S: 2.19–2.84 Å, Figure S9a) and Ag···Ag interactions. Dissimilarly, for **SD/Ag54b**, an Ag_6S_6 core is enclosed in the Ag_{30} cage (Figure 2e), where six S^{2-} ions link them together (Ag–S: 2.42–2.88 Å) with the assistance of Ag···Ag interactions (Ag···Ag: 2.97–3.29 Å, Figure S9b). These inner S^{2-} ions should be generated from partial decomposition of $Ph_2PS_2^-$ [36]. Why can the similar silver cage accommodate silver core of different sizes inside? The flexibility of Ag_{30} cage may address this issue. In details, six S^{2-} ions in both Ag_7S_6 and Ag_6S_6 can form a S_6 octahedron (Figure S10) where the average S–S edge length in Ag_7S_6 (4.76 Å) is 0.31 Å longer than that in Ag_6S_6 (4.45 Å), suggesting a larger core in **SD/Ag55b**. To accommodate the larger core, the outer Ag_{30} cage in **SD/Ag55b** becomes larger than that in **SD/Ag54b**, reflected by the longer average Ag···Ag separations in the shell of **SD/Ag55b** (3.06 Å for **SD/Ag55b** and 3.03 Å for **SD/Ag54b**). On the basis of the compared structural and synthetic details, although alkynes didn't directly participate in protecting silver cores of **SD/Ag55b** and **SD/Ag54b**, we propose that the substituted groups on alkynes influence the size and geometry of silver core during the growth incipient stage in a non-invasive fashion.

Interestingly, all ligands in **SD/Ag55b** and **SD/Ag54b** have almost the same surface distributions and coordination modes. Here, we take **SD/Ag55b** as an example. The *p*-MePhC≡C$^-$ and $Ph_2PS_2^-$ are in a staggered arrangement with

the latter located at the poles and the equator and the former dispersing in between. Each $Ph_2PS_2^-$ ligand caps on the silver tetragons of the Ag_{48} shell using a μ_4 coordination mode (Ag–S: 2.50–2.66 Å, Figure S11). The 24 *p*-MePhC≡C$^-$ ligands can be divided into six groups located at six different regions with each containing 3, 6, 3, 3, 6 and 3 *p*-MePhC≡C$^-$ ligands, respectively. Notably, all *p*-MePhC≡C$^-$ ligands are anchored to the silver trigons of the Ag_{48} shell (μ_3-η^1:η^1:η^1, Ag–C: 2.09–2.46 Å, Figure S12).

In all, the nine *p*-MePhC≡C$^-$ and three $Ph_2PS_2^-$ ligands co-protect the Ag_{15} cage (Figure S13), whereas the Ag_{30} cage in the waist is co-protected by six *p*-MePhC≡C$^-$ and six $Ph_2PS_2^-$ ligands (Figure S14). The three cages fused together to accomplish the overall Ag_{55} cluster through face-sharing hexagons. More interesting, the coordination regioselectivity of $Ph_2PS_2^-$ and RC≡C$^-$ ligands synergistically shapes the polyhedral Ag_{48} shell by exclusively fabricating silver tetragons and trigons, respectively.

2.3 NMR and mass spectrometry of SD/Ag55b and SD/Ag54b

To check the solution behavior of **SD/Ag55b**, we examined the NMR spectroscopies by dissolving the crystals in dichloromethane-d_2. The peaks in the range of 5.77–7.74 ppm correspond to the protons on the phenyl groups of both *p*-MePhC≡C$^-$ and $Ph_2PS_2^-$ ligands, whereas those in 1.59–2.37 ppm are solely assigned to the protons on the methyl groups of the *p*-MePhC≡C$^-$ ligands. The integral ratio of phenyl and methyl protons is 3:1.19 (Figure S15a), which is in good agreement with the theoretical ratio of 3:1 ((24×4+12×10): (24×3)) in the molecular structure in solid state, confirming the composition and purity of the crystals. Moreover, ^{31}P NMR spectrum of **SD/Ag55b** shows two sets of resonance peaks at 71.81 and 66.41 ppm with an equal integral area (Figure S15b), which confirms that there are two different $Ph_2PS_2^-$ ligands of equal quantity on **SD/Ag55b**. This is consistent with the observation of $Ph_2PS_2^-$ ligands equally distributed at the polar and equatorial positions of **SD/Ag55b**. The ^{31}P NMR of free $Ph_2PS_2{\cdot}HNEt_3$ ligand [50] (δ = 62.6 ppm) is quite different from that of **SD/Ag55b**, which also proves that $Ph_2PS_2^-$ ligand is ligated to the mother cluster instead of an unbound state in the solution. All these NMR results undoubtedly confirm that **SD/Ag55b** remains structurally intact in CH_2Cl_2. Due to the very low solubility of **SD/Ag54b**, no useful NMR signals can be detected by dissolving it in most common solvents. In order to prove the counter-anion to be $CF_3SO_3^-$ in **SD/Ag54b**, the ^{19}F NMR was measured after the crystal was digested with excessive HNO_3 (31.68%), which showed a sharp peak at −78.91 ppm, consistent with the ^{19}F chemical shift of $CF_3SO_3^-$ reported in the literatures (Figure S16) [54,55]. The result confirmed there are $CF_3SO_3^-$ counterions in the lattice of **SD/Ag54b**, which balanced the positive charge on the cluster.

The solution behaviors of **SD/Ag55b** and **SD/Ag54b** were further investigated in CH_2Cl_2 using electrospray ionization mass spectrometry (ESI-MS). ESI-MS was performed in both positive and negative ion modes, but only positive mode ESI-MS provides useful signals. The ESI-MS of **SD/Ag55b** is quite clean with only one sharp peak (**1a**) at *m*/*z* = 4,066.8760 in the range of 2,000–5,000 (Figure 3a). This predominant peak was assigned to the molecular ion of **SD/Ag55b**, $[Ag_7S_6@Ag_{48}(MoO_4)_2(p\text{-MePhC}{\equiv}C)_{24}(Ph_2PS_2)_{12}]^{3+}$ (Calcd *m*/*z* = 4,066.8830), which suggests the high stability of **SD/Ag55b** in CH_2Cl_2. Of note, it also confirms that all the Ag atoms are in +1 oxidation state, suggesting that Ag_7 core is not a subvalent silver kernel. When increasing the source voltage and dry temperature, this molecular ion peak of **SD/Ag55b** is still there and no fragmented species are found (Figure S17), which indicates that **SD/Ag55b** is robust even under harsh conditions.

Differently, a slightly widened doubly charged envelope (**2a**–**2c**) was detected in the *m*/*z* range of 4,000–7,000 for **SD/Ag54b** in CH_2Cl_2 (Figure S18), which contains a main component **2a** ($[Ag_6S_6@Ag_{48}(MoO_4)_2(PhC{\equiv}C)_{24}(Ph_2PS_2)_{12}]^{2+}$) centered at *m*/*z* = 5,877.6717, corresponding to the molecular ion peak of **SD/Ag54b** (Calcd 5,877.6840) based on the well-matched experimental and calculated isotope distributions. The **2b** and **2c** at *m*/*z* = 5,870.6608 and 5,886.6569 are assigned to $[Ag_6S_6@Ag_{48}(MoO_4)_2(PhC{\equiv}C)_{24}(Ph_2PS_2)_{11}(CF_3SO_3)(CH_3OH)(H_2O)_3]^{2+}$, (Calcd 5,870.6908) and $[Ag_6S_6@Ag_{48}(MoO_4)_2(PhC{\equiv}C)_{24}(Ph_2PS_2)_{12}(H_2O)]^{2+}$ (Calcd 5,886.6893), respectively. So similar to **SD/Ag55b**, all the Ag atoms of **SD/Ag54b** are also in +1 oxidation state. These results demonstrate that **SD/Ag54b** still remain metal skeleton intact in CH_2Cl_2, although the ligand and solvent exchange occurs in some extent.

Mass spectrometry is also a powerful tool to study the reactivity of the cluster and monitor such process in detail [56,57]. We used mass spectrometry to real-time monitor the ligand exchange process of **SD/Ag55b** in detail. In a screw-sealed glass vial, 2 mg of crystals of **SD/Ag55b** were dissolved in 8 mL CH_2Cl_2 and then mixed with 132 μL *c*PrC≡CH. Then the resulting mixture was stirred at room temperature. We extracted 20 μL of the mixed solution using a micropipette every 1 h and diluted it with 1 mL CH_2Cl_2, and then transferred it to mass spectrometer. There is only the molecular ion peak of **SD/Ag55b** without *c*PrC≡CH added at the beginning (Figure 3b). After adding *c*PrC≡CH, the intensity of molecular ion peak of **SD/Ag55b** gradually decreases and becomes almost negligible after 4 h. Meanwhile, a series of overlapped peaks appear in the lower *m*/*z* range. At last, a single peak corresponding to completely *c*PrC≡C$^-$ substituted **SD/Ag55b** is left after 10 h (Figure 3c).

Expanding each peak and checking the spacing between

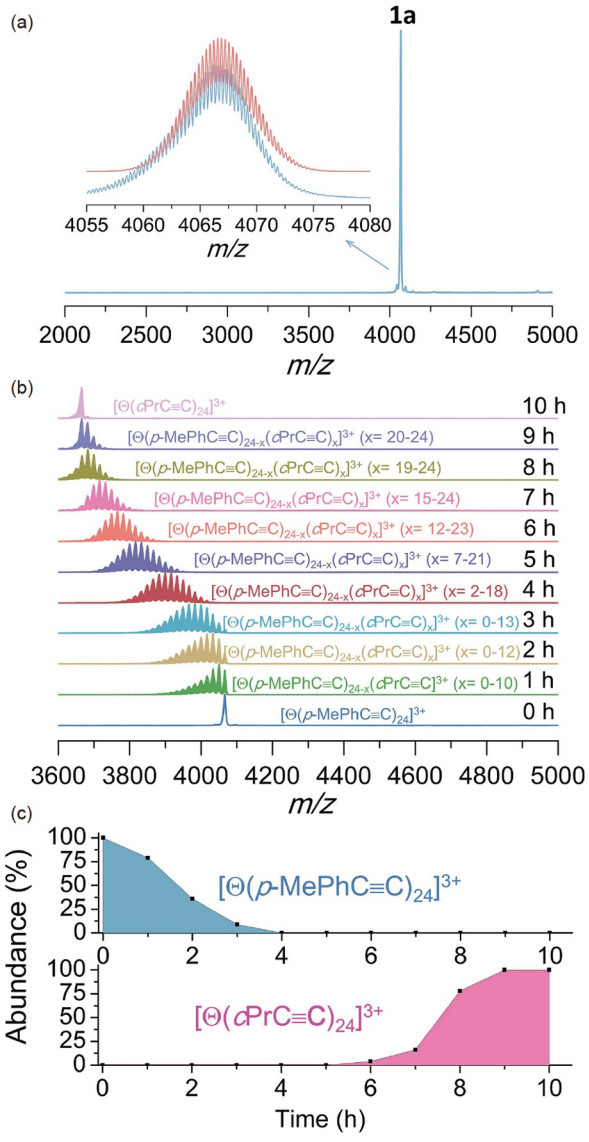

Figure 3 (a) Positive ion mode ESI-MS of **SD/Ag55b** dissolved in CH_2Cl_2 showing one main peaks. The insets are superimposed experimental (blue) and simulated (red) isotopic patterns for the species. (b) Time-course ESI-MS of formation of $[\Theta(c\text{PrC}{\equiv}\text{C})_{24}]^{3+}$ (Θ = $(MoO_4)_2S_6Ag_{55}(Ph_2PS_2)_{12}$) from $[\Theta(p\text{-MePhC}{\equiv}\text{C})_{24}]^{3+}$. (c) Time-dependent abundance evolution of $[\Theta(p\text{-MePhC}{\equiv}\text{C})_{24}]^{3+}$ and $[\Theta(c\text{PrC}{\equiv}\text{C})_{24}]^{3+}$ (color online).

adjacent isotopic peaks, we found that these peaks carry three positive charges, and the *m*/z interval between two adjacent peaks is equal to the mass difference of *p*-MePhC≡C$^-$ and *c*PrC≡C$^-$ (ΔM_W = 50.0156) divided by the 3, which indicates that the exchange between alkyne ligands occurs. Their precise formula were assigned based on the good agreement between the observed and simulated isotopic distribution patterns.

In detail, after one hour reaction with *c*PrC≡CH, original single peak was transformed to a group of peaks. The intensities of the peaks don't fit the Gaussian distribution, and a closer analysis revealed that they consist of at least ten species, which are assigned to $[\Theta(p\text{-MePhC}{\equiv}\text{C})_{24-x}(c\text{PrC}{\equiv}\text{C})_x]^{3+}$ (Θ = $Ag_{55}S_6(MoO_4)_2(Ph_2PS_2)_{12}$, x = 1, 2, 3……10). The most abundant species at m/z = 4,050.1963 can be assigned to $[\Theta(p\text{-MePhC}{\equiv}\text{C})_{24-1}(c\text{PrC}{\equiv}\text{C})_1]^{3+}$ (Figure S19a), and every two adjacent species at lower m/z range were generated by replacing one *p*-MePhC≡C$^-$ by one *c*PrC≡C$^-$ ligand. The total profile of these grouped peaks is basically in accordance with the Gaussian distribution after 4-h reaction. The most dominated species are $[\Theta(p\text{-MePhC}{\equiv}\text{C})_{24-x}(c\text{PrC}{\equiv}\text{C})_x]^{3+}$ (x = 9, 13, 17) (Figure S19d–f), indicating that 9, 13 and 17 *p*-MePhC≡C$^-$ have been replaced by *c*PrC≡C$^-$, respectively, after reacting for 4, 5 and 6 h. Along the reaction going on, more and more *c*PrC≡C$^-$ replace *p*-MePhC≡C$^-$. Until reacting for 10 h, only one peak at m/z = 3,666.4378 was observed, which can be assigned to $[\Theta(c\text{PrC}{\equiv}\text{C})_{24}]^{3+}$ (Calcd 3,666.4233, Figure S20). The kinetics of ligand exchange reaction on the surface of nanoclusters was also studied and the details are in the Figure S21. These dynamic phenomena in the process of ligand exchange indicated that (i) the occurrence of ligand exchange in **SD/Ag55b** is a time-dependent process; (ii) the completely substituted product can be obtained finally; (iii) the binding of $Ph_2PS_2^-$ to silver nanocluster is quite strong and is not influenced by such a ligand exchange process, and (iv) the metal core can keep intact during ligand exchange. The real-time ESI-MS monitoring approach developed in this study could also be extended to other ligand exchange systems to reveal the reaction dynamics of ligands on the surface of metal cluster as well as mechanism aspects. We also envisaged that the ligand exchange approach may modify the surface structure and the fraction of ligand coverage, bringing new functionality to silver nanoclusters.

2.4 Photoluminescence properties of SD/Ag55b and SD/Ag54b

The photoluminescence of **SD/Ag55b** and **SD/Ag54b** was studied in CH_2Cl_2 solution at room temperature. **SD/Ag54b** emits orange-red light with an emission maximum at 622 nm excited by 365 nm. In contrast, **SD/Ag55b** displays a lower energy band emission under the same excitation wavelength, which has a 40 nm red-shift compared with **SD/Ag54b** (Figure 4a). The luminescence lifetimes of **SD/Ag55b** and **SD/Ag54b** at 293 K are 95.35 and 985.90 ns, respectively (Figure 4b). The 10-fold shorter lifetime of **SD/Ag55b** should be caused by additional CH_3 groups on phenylacetylene that accelerate the irradiation deactivation process through the rotation motions. The large Stokes shift of ~250 nm (Figure S22) and the long lifetimes imply the origin of triplet excited states [58–60]. These emissions should be tentatively attributed to ligand-to-metal-charge-transfer (^{3}LMCT) transition from the RC≡C$^-$ and $Ph_2PS_2^-$ to Ag atoms mixed with cluster-center (^{3}CC) transitions [61]. However, considering their similar shell structures, we can reasonably assign the red-shifted

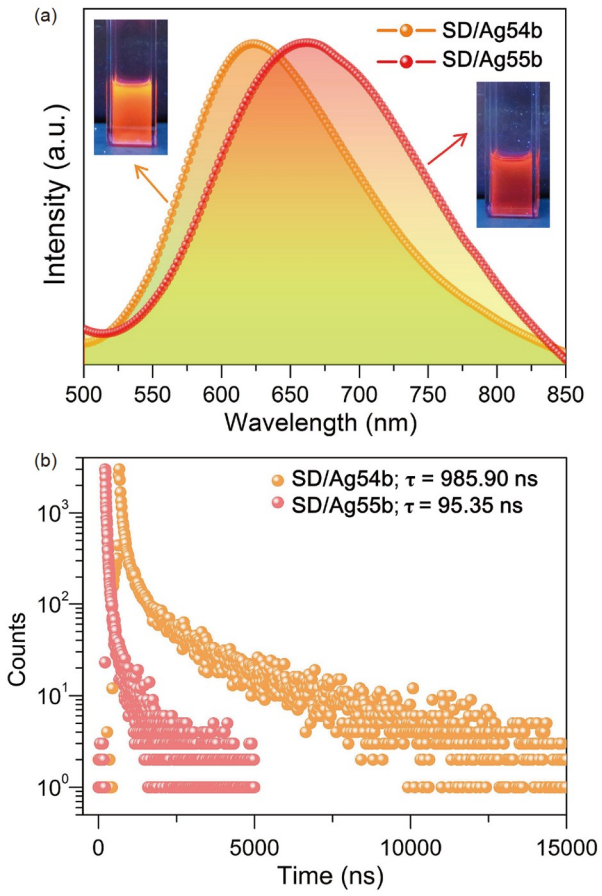

Figure 4 (a) The emission spectra of **SD/Ag55b** and **SD/Ag54b** in CH_2Cl_2 (1.3×10^{-4} mol L^{-1}) under 365 nm excitation. Insets: the photographs of **SD/Ag55b** and **SD/Ag54b** under 365 nm UV light at room temperature. (b) Emission decay of **SD/Ag55b** and **SD/Ag54b** in the CH_2Cl_2 at 293 K (color online).

behavior to their different core structures [62,63]. In detail, **SD/Ag55b** has a larger Ag_7 core that possesses more and stronger Ag···Ag interactions (average Ag···Ag distance: 3.03 Å) compared to the smaller Ag_6 core (average Ag···Ag distance: 3.12 Å) in **SD/Ag54b**. Due to the similar Ag_{48} outer shell, the larger core structure, the stronger confinement effect of inner space, which surely compresses Ag···Ag distances in the core, producing stronger argentophilic interactions [64]. As we know, ^{3}CC transition state is predominately controlled by argentophilic interactions, and therefore the more and stronger argentophilic interactions can effectively lower the energy level of ^{3}CC transition state, producing the red-shifted emission for **SD/Ag55b**.

In addition, in order to further eliminate the effects of cluster aggregation on the photoluminescence of **SD/Ag55b** and **SD/Ag54b** in crystalline state, the emission spectra of them in dilute solutions of three different concentrations (c_1 = 1.3×10^{-4} mol L^{-1}, c_2 = 3.5×10^{-5} mol L^{-1}, c_3 = 7.0×10^{-6} mol L^{-1}) were obtained in detail, respectively. It was found that the emission maximum was not concentration-dependent (Figure S23). These emission spectra obtained in extremely dilute solution approximately represented the intrinsic emission properties of single cluster, which ruled out the influences from aggregation of clusters on the photoluminescence when they are in solid state or concentrated solution. Further, the luminescence in solid state at room temperature of **SD/Ag54b** and **SD/Ag55b** shows emission maxima at 625 and 656 nm, respectively, which is basically the same with the isolated clusters in solution (Figure S24). All these results evidence that the red-shifted emission of **SD/Ag55b** is genuinely attributed to the more and stronger argentophilic interactions of the Ag_7 core. The work provides us a rare pair of comparable examples to reveal precise structure-function relationships. Based on above good emissive properties of **SD/Ag55b**, we also attempt to fabricate white light-emitting diode (WLED) devices using the commercial blue phosphor and **SD/Ag55b**, as details shown in Figure S25.

3 Conclusions

In conclusion, we synthesized and characterized two silver nanoclusters synergistically constructed by $RC{\equiv}C^-/Ph_2PS_2^-$ ligands. The $RC{\equiv}C^-$ and $Ph_2PS_2^-$ ligands play crucial roles in shaping silver trigons and tetragons, respectively, which then build the polyhedral silver nanoclusters. The latter also behaves as sulfur-releasing agent to form the central $[Ag_mS_6]$ cores. Specially, two silver nanoclusters have a similar Ag_{48} shell that however encages different cores, which should be dictated by alkyne ligand with different substitution groups. Although no directly binding between organic ligand and core was found in final structures, alkyne ligands possibly impact the incipient nucleation growth of metal core in a non-invasive manner, which helps us to understand the elusive core modulation details in core-shell silver nanoclusters. The bulk alkyne ligands on the shell can be completely exchanged by a smaller one within 10 h at room temperature, as revealed by time-dependent mass spectrometry, which may be beneficial to exposing the potential catalytic sites by reducing the steric congestion on the ligand shell. The core structure in silver nanocluster with more and stronger argentophilic interactions will trigger lower energy emission by correlating their structures and luminescent properties. We believe the synergistic effect of $RC{\equiv}C^-/Ph_2PS_2^-$ ligands and the insights about core regulation by alkyne ligands could provide some fundamental understanding about the rationally assembly and related properties of core-shell silver nanoclusters.

Acknowledgements This work was supported by the National Natural Science Foundation of China (91961105, 21822107), the Fok Ying Tong Education Foundation (171009), the Natural Science Foundation of Shandong Province (ZR2019ZD45, ZR2020ZD35, JQ201803, ZR2017MB061), the Taishan Scholar Project of Shandong Province of China

(tsqn201812003, ts20190908), the Qilu Youth Scholar Funding of Shandong University, and Project for Scientific Research Innovation Team of Young Scholar in Colleges and Universities of Shandong Province (2019KJC028).

Conflict of interest The authors declare no conflict of interest.

Supporting information The supporting information is available online at http://chem.scichina.com and http://link.springer.com/journal/11426. The supporting materials are published as submitted, without typesetting or editing. The responsibility for scientific accuracy and content remains entirely with the authors.

1 Ueda M, Goo ZL, Minami K, Yoshinari N, Konno T. *Angew Chem Int Ed*, 2019, 58: 14673–14678
2 Zhang S, Zhao L. *Acc Chem Res*, 2018, 51: 2535–2545
3 Ott LS, Finke RG. *Coord Chem Rev*, 2007, 251: 1075–1100
4 Zarra S, Wood DM, Roberts DA, Nitschke JR. *Chem Soc Rev*, 2015, 44: 419–432
5 Joshi CP, Bootharaju MS, Alhilaly MJ, Bakr OM. *J Am Chem Soc*, 2015, 137: 11578–11581
6 Schnepf A, Schnöckel H. *Angew Chem Int Ed*, 2014, 53: 3064–3066
7 Kondo J, Tada Y, Dairaku T, Hattori Y, Saneyoshi H, Ono A, Tanaka Y. *Nat Chem*, 2017, 9: 956–960
8 Kovalenko MV, Scheele M, Talapin DV. *Science*, 2009, 324: 1417–1420
9 He L, Yuan J, Xia N, Liao L, Liu X, Gan Z, Wang C, Yang J, Wu Z. *J Am Chem Soc*, 2018, 140: 3487–3490
10 Shen H, Kubo K, Kume S, Zhang L, Mizuta T. *Dalton Trans*, 2017, 46: 16199–16204
11 Qu M, Li H, Xie LH, Yan ST, Li JR, Wang JH, Wei CY, Wu YW, Zhang XM. *J Am Chem Soc*, 2017, 139: 12346–12349
12 Lei Z, Wan XK, Yuan SF, Guan ZJ, Wang QM. *Acc Chem Res*, 2018, 51: 2465–2474
13 Yao Q, Chen T, Yuan X, Xie J. *Acc Chem Res*, 2018, 51: 1338–1348
14 Xie YP, Jin JL, Duan GX, Lu X, Mak TCW. *Coord Chem Rev*, 2017, 331: 54–72
15 Wang QM, Lin YM, Liu KG. *Acc Chem Res*, 2015, 48: 1570–1579
16 Yam VWW. *Acc Chem Res*, 2002, 35: 555–563
17 Rais D, Yau J, Mingos DMP, Vilar R, White AJP, Williams DJ. *Angew Chem Int Ed*, 2001, 40: 3464–3467
18 Gruber F, Jansen M. *Angew Chem Int Ed*, 2010, 49: 4924–4926
19 Xie YP, Mak TCW. *J Am Chem Soc*, 2011, 133: 3760–3763
20 Bian SD, Jia JH, Wang QM. *J Am Chem Soc*, 2009, 131: 3422–3423
21 Li S, Du XS, Li B, Wang JY, Li GP, Gao GG, Zang SQ. *J Am Chem Soc*, 2018, 140: 594–597
22 Huang RW, Wei YS, Dong XY, Wu XH, Du CX, Zang SQ, Mak TCW. *Nat Chem*, 2017, 9: 689–697
23 Narouz MR, Osten KM, Unsworth PJ, Man RWY, Salorinne K, Takano S, Tomihara R, Kaappa S, Malola S, Dinh CT, Padmos JD, Ayoo K, Garrett PJ, Nambo M, Horton JH, Sargent EH, Häkkinen H, Tsukuda T, Crudden CM. *Nat Chem*, 2019, 11: 419–425
24 Chen YT, Krytchankou IS, Karttunen AJ, Grachova EV, Tunik SP, Chou PT, Koshevoy IO. *Organometallics*, 2017, 36: 480–489
25 Sharma S, Chakrahari KK, Saillard JY, Liu CW. *Acc Chem Res*, 2018, 51: 2475–2483
26 Rothenberger A, Shafaei-Fallah M, Shi W. *Chem Commun*, 2007, 1499–1501
27 Lobana T, Wang J, Liu C. *Coord Chem Rev*, 2007, 251: 91–110
28 Dhayal RS, Liao JH, Liu YC, Chiang MH, Kahlal S, Saillard JY, Liu CW. *Angew Chem Int Ed*, 2015, 54: 3702–3706
29 Dhayal RS, Lin YR, Liao JH, Chen YJ, Liu YC, Chiang MH, Kahlal S, Saillard JY, Liu CW. *Chem Eur J*, 2016, 22: 9943–9947
30 Liu CW, Lin YR, Fang CS, Latouche C, Kahlal S, Saillard JY. *Inorg Chem*, 2013, 52: 2070–2077
31 Chang HW, Shiu RY, Fang CS, Liao JH, Kishore PVVN, Kahlal S, Saillard JY, Liu CW. *J Clust Sci*, 2017, 28: 679–694
32 Edwards AJ, Dhayal RS, Liao PK, Liao JH, Chiang MH, Piltz RO, Kahlal S, Saillard JY, Liu CW. *Angew Chem Int Ed*, 2014, 53: 7214–7218
33 Dhayal RS, Liao JH, Kahlal S, Wang X, Liu YC, Chiang MH, van Zyl WE, Saillard JY, Liu CW. *Chem Eur J*, 2015, 21: 8369–8374
34 Chiu TH, Liao JH, Gam F, Chantrenne I, Kahlal S, Saillard JY, Liu CW. *J Am Chem Soc*, 2019, 141: 12957–12961
35 Barik SK, Chiu TH, Liu YC, Chiang MH, Gam F, Chantrenne I, Kahlal S, Saillard JY, Liu CW. *Nanoscale*, 2019, 11: 14581–14586
36 Shafaei-Fallah M, Anson CE, Fenske D, Rothenberger A. *Dalton Trans*, 2005, 2300–2304
37 Shi W, Ahlrichs R, Anson CE, Rothenberger A, Schrodt C, Shafaei-Fallah M. *Chem Commun*, 2005, 1: 5893–5895
38 Chakrahari KK, Liao JH, Kahlal S, Liu YC, Chiang MH, Saillard JY, Liu CW. *Angew Chem Int Ed*, 2016, 55: 14704–14708
39 Silalahi RPB, Chakrahari KK, Liao JH, Kahlal S, Liu YC, Chiang MH, Saillard JY, Liu CW. *Chem Asian J*, 2018, 13: 500–504
40 Wang Z, Su HF, Kurmoo M, Tung CH, Sun D, Zheng LS. *Nat Commun*, 2018, 9: 2094
41 Su YM, Wang Z, Zhuang GL, Zhao QQ, Wang XP, Tung CH, Sun D. *Chem Sci*, 2019, 10: 564–568
42 Wang Z, Qu QP, Su HF, Huang P, Gupta RK, Liu QY, Tung CH, Sun D, Zheng LS. *Sci China Chem*, 2020, 63: 16–20
43 Wang Z, Sun HT, Kurmoo M, Liu QY, Zhuang GL, Zhao QQ, Wang XP, Tung CH, Sun D. *Chem Sci*, 2019, 10: 4862–4867
44 Wang Z, Yang FL, Yang Y, Liu QY, Sun D. *Chem Commun*, 2019, 55: 10296–10299
45 Wang Z, Su HF, Zhuang GL, Kurmoo M, Tung CH, Sun D, Zheng LS. *CCS Chem*, 2019, 1: 663–672
46 Liu JW, Wang Z, Chai YM, Kurmoo M, Zhao QQ, Wang XP, Tung CH, Sun D. *Angew Chem Int Ed*, 2019, 58: 6276–6279
47 Li G, Lei Z, Wang QM. *J Am Chem Soc*, 2010, 132: 17678–17679
48 Nan ZA, Wang Y, Chen ZX, Yuan SF, Tian ZQ, Wang QM. *Commun Chem*, 2018, 1: 99
49 Wang Z, Liu JW, Su HF, Zhao QQ, Kurmoo M, Wang XP, Tung CH, Sun D, Zheng LS. *J Am Chem Soc*, 2019, 141: 17884–17890
50 Wagner J, Ciesielski M, Fleckenstein CA, Denecke H, Garlichs F, Ball A, Doering M. *Org Process Res Dev*, 2013, 17: 47–52
51 Schmidbaur H, Schier A. *Angew Chem Int Ed*, 2015, 54: 746–784
52 Wu XH, Wei Z, Yan BJ, Huang RW, Liu YY, Li K, Zang SQ, Mak TCW. *CCS Chem*, 2019, 1: 553–560
53 Zhang SS, Alkan F, Su HF, Aikens CM, Tung CH, Sun D. *J Am Chem Soc*, 2019, 141: 4460–4467
54 Pluta R, Nikolaienko P, Rueping M. *Angew Chem Int Ed*, 2014, 53: 1650–1653
55 Blanco MC, Cámara J, Gimeno MC, Laguna A, James SL, Lagunas MC, Villacampa MD. *Angew Chem Int Ed*, 2012, 51: 9777–9779
56 Zheng K, Fung V, Yuan X, Jiang DE, Xie J. *J Am Chem Soc*, 2019, 141: 18977–18983
57 Li Y, Juarez-Mosqueda R, Song Y, Zhang Y, Chai J, Mpourmpakis G, Jin R. *Nanoscale*, 2020, 12: 9423–9429
58 Yu H, Rao B, Jiang W, Yang S, Zhu M. *Coord Chem Rev*, 2019, 378: 595–617
59 Yang H, Lei J, Wu B, Wang Y, Zhou M, Xia A, Zheng L, Zheng N. *Chem Commun*, 2013, 49: 300–302
60 Zhang R, Zhao C, Li X, Zhang Z, Ai X, Chen H, Cao R. *Dalton Trans*, 2016, 45: 12772–12778
61 Yam VWW, Au VKM, Leung SYL. *Chem Rev*, 2015, 115: 7589–7728
62 Dimuthu KL, Weerawardene M, Aikens CM. *J Am Chem Soc*, 2016, 138: 11202–11210
63 Udaya Bhaskara Rao T, Pradeep T. *Angew Chem Int Ed*, 2010, 49: 3925–3929
64 Grandjean D, Coutiño-Gonzalez E, Cuong NT, Fron E, Baekelant W, Aghakhani S, Schlexer P, D'Acapito F, Banerjee D, Roeffaers MBJ, Nguyen MT, Hofkens J, Lievens P. *Science*, 2018, 361: 686–690